Improving representation of riparian vegetation shading in a regional stream temperature model using LiDAR data

Loicq, Pierre; Moatar, Florentina; Jullian, Yann; Dugdale, Stephen J.; Hannah, David M.

DOI:
10.1016/j.scitotenv.2017.12.129

Improving representation of riparian vegetation shading in a regional stream temperature model using LiDAR data

Pierre Loicq[a,*], Florentina Moatar[a], Yann Jullian[b], Stephen J. Dugdale[c], David M. Hannah[c]

[a] *EA 6293 GéHCO Géo-Hydrosystèmes Continentaux, Université François-Rabelais de Tours, Parc de Grandmont 37200 Tours, France*
[b] *CaSciModOT, UFR Sciences et Techniques, Université François Rabelais, Parc de Grandmont 37200 Tours, France*
[c] *School of Geography, Earth and Environmental Sciences, University of Birmingham, Edgbaston, Birmingham B15 2TT, United Kingdom*

*Corresponding author. E-mail address: pierre.loicq@univ-tours.fr

Keywords: river temperature modelling, regional scale, riparian shading, LiDAR, Loir River.

Highlights:

- Riparian shading was characterised on a 270 km stream using LiDAR data.
- Shading data were injected in a regional stream temperature model.
- Vegetation's cooling effect ranges from -3.0 °C (upstream) to -1.3 °C (downstream).
- Model accuracy is improved compared to simpler shade characterisation methods.
- Riparian vegetation data's quality is a key factor for stream temperature modelling.

Graphical abstract:

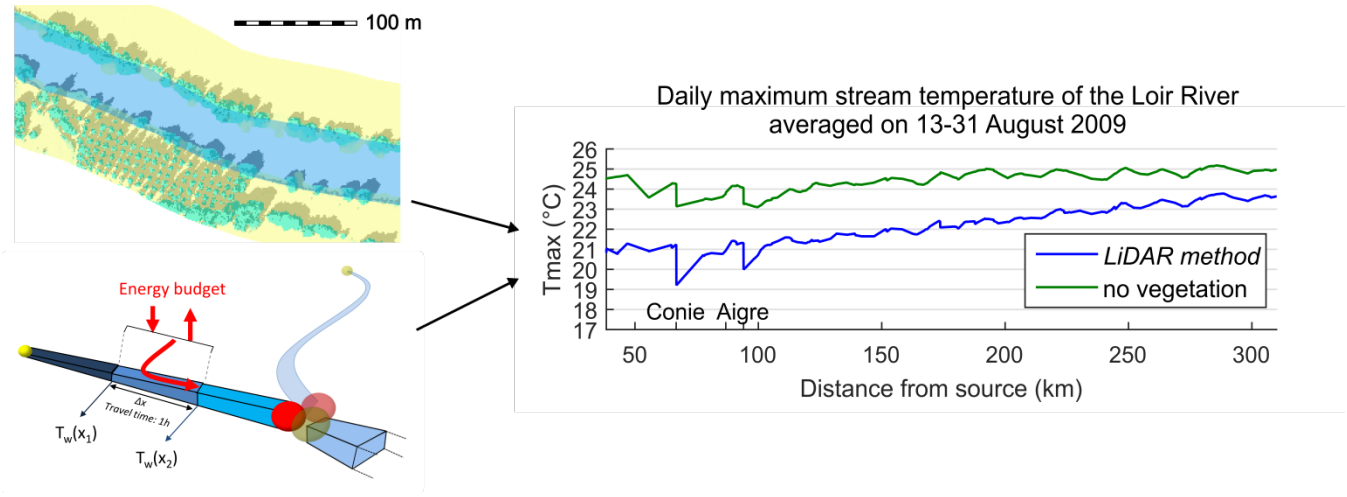

Abstract

Modelling river temperature at the catchment scale is needed to understand how aquatic communities may adapt to current and projected climate change. In small and medium rivers, riparian vegetation can greatly reduce maximum water temperature by providing shade. It is thus important that river temperature models are able to correctly characterise the impact of this riparian shading. In this study, we describe the use of a spatially-explicit method using LiDAR-derived data for computing the riparian shading on direct and diffuse solar radiation. The resulting data are used in the T-NET one-dimensional stream temperature model to simulate water temperature from August 2007 to July 2014 for 270 km of the Loir River, an indirect tributary of the Loire River (France). Validation is achieved with 4 temperature monitoring stations spread along the Loir River. The vegetation characterised with the LiDAR approach provides a cooling effect on maximum daily temperature (T_{max}) ranging from 3.0°C (upstream) to 1.3°C (downstream) in late August 2009. Compared to two other riparian shading routines that are less computationally-intensive, the use of our LiDAR-based methodology improves the

bias of T_{max} simulated by the T-NET model by 0.62°C on average between April and September. However, difference between the shading routines reaches up to 2°C (monthly average) at the upstream-most station. Standard deviation of errors on T_{max} is not improved. Computing the impact of riparian vegetation at the hourly timescale using reach-averaged parameters provides results close to the LiDAR-based approach, as long as it is supplied with accurate vegetation cover data. Improving the quality of riparian vegetation data should therefore be a priority to increase the accuracy of stream temperature modelling at the regional scale.

1. Introduction

Temperature is a major water quality parameter because it controls not only oxygen solubility (Moatar et al., 2001) but also chemical and metabolic reactions (Haag and Westrich, 2002). Hence, it affects fish behaviour and survival (Magnuson et al., 1979). River water temperature modelling is thus important for understanding the distribution of aquatic species at regional scales, under present or future climatic conditions (Buisson et al., 2008; Tisseuil et al., 2012; Boisneau et al., 2008; Brown et al., 2005). River temperature is already increasing across French water courses, a trend which is expected to continue further under projected climate change (Moatar and Gailhard, 2006; Bustillo et al., 2014; Hannah and Garner, 2015). Such a warming could have severe consequences for a range of aquatic species, and adaptation measures are currently being sought with a view to ensuring the continued survival of temperature sensitive fluvial organisms. In this context, riparian shade and groundwater exchanges have been given increasing research attention, because of their ability to regulate river temperature (Lalot et al., 2015; Leach and Moore, 2010). Indeed, many studies have shown that shade can moderate water temperature of relatively small rivers (Moore et al., 2005; Garner et al., 2014). Conversely, in larger rivers, Teti (2006) showed (using shade measurements acquired along an increasing-width stream) that riparian vegetation has a limited impact on rivers larger than 30 m. DeWalle (2008) quantified the maximal wetted width for which riparian vegetation can effectively reduce received solar radiation. However, no study has yet quantified the impact of shading on temperature on rivers of intermediate width (>15 m and <30 m) or at the regional scale.

Process-based river temperature models function by simulating the energy exchange processes heating or cooling a river, in particular through the input of solar radiation. This solar radiation is composed of direct (solar rays) and diffuse radiation (scattered by atmosphere), both of which are influenced in different ways by the presence of riparian vegetation. The impact of riparian vegetation on the direct radiation can be quantified by computing a shadow factor (SF), which is the proportion of a river being shaded at a given time. Several methods have been proposed to compute it at an hourly time step. Chen et al. (1998) detailed a method to compute riparian shade from GIS polygons of riparian vegetation. Their method used stream azimuth and tree height (alongside solar position) to determine whether a section of stream channel was in shade. However, this technique only accounted for the effect of vegetation located perpendicular to the stream centreline, and furthermore, did not denote the fraction of the channel cross-section that was shaded. As a result, Li et al. (2012) developed an enhanced version of the Chen et al. (1998) methodology, allowing for the determination of the amount of channel cross-section covered by shade. This new method also enables the simulation of

overhanging vegetation, but like its predecessor, only considers the effect of vegetation located perpendicular to the river reach. Approaches capable of simulating the effects of vegetation non-perpendicular to the reach include that of Cox and Bolte (2007), who devised a methodology capable of simulating shadow cast by vegetation located in 8 directions (steps of 45°) around each centreline node, and the Solar Analyst extension for ArcGIS (Fu and Rich, 1999), which can compute shadow factor at much finer spatial and temporal scales. Indeed, Johnson and Wilby (2015) applied this method to a small catchment in order to quantify the potential of planting trees, without using a physically-based river temperature model.

The impact of riparian vegetation on diffuse radiation can be quantified by computing a sky view factor (SVF). It is the ratio between the diffuse radiation actually reaching the water and the diffuse radiation that would reach this surface with no vegetation around. In a lowland area where topographic shade can be neglected, the tree view factor (TVF) can be defined as 1-SVF. Unlike SF, these view factors (VF) are constant in time since they do not depend on the sun's position. For short reaches, a precise calculation can be achieved through hemispheric photography. For larger areas, remote sensing products or vegetation polygons are needed. Most previous studies (Chen et al., 1998, Cox and Bolte, 2007, Loinaz et al., 2013, Sun et al., 2015) simply use the angle between the horizon and the tree in the directions perpendicular to the river, from one fixed point of view (usually the centre of the river). Moore et al. (2014) introduced the computation of width-averaged sky view factors, with equations considering infinitely long rivers, with or without overhanging trees.

With an approach similar to the one used to compute direct radiation, the Solar Analyst extension for ArcGIS handles the computation of diffuse radiation by overlaying a viewshed and a discretised sky map. Two different methods can be used to quantify the amount of radiation coming from each cell of the open sky (uniform radiation or depending on the zenith angle). This method was modified and used by Sridhar et al. (2004) to include the shading effects of near stream vegetation.

In order to quantify the impact of riparian shading, existing regional-scale stream temperature models usually rely on theoretical values regarding vegetation characteristics (Sun et al., 2015; Loinaz et al., 2013), on simplified assumptions regarding shading process (Haag and Luce, 2008; Cheng and Wiley, 2016), or incorporate shading data from low-resolution DEMs (Cox and Bolte, 2007). Nowadays however, LiDAR can provide accurate data at a large scale. In order to develop a tool for riparian shade inventories using LiDAR data, Guzy et al. (2015) adapted the insolation module of the Heat Source model (Boyd and Kasper, 2003). They created polygons of homogenous potential canopy height and extracted the 75^{th} percentile of the computed frequency distribution of canopy height provided by LiDAR. Greenberg et al. (2012) used LiDAR data and the r.sun module of GRASS GIS to compute clear-sky solar radiation for three summer days in order to understand the impact of a potential trees removal around a delta, without the use of a network based temperature model. Finally, Wawrzyniak et al. (2017) used LiDAR data to compute the impact of riparian forest in a deterministic water temperature model of a 21 km-long reach, during 5 days in summer 2010 and 2011. There is thus a range of data sources and methods available to compute both SF and VF. However, there remains a lack of information comparing the various methodologies, especially with regards to shading routines in regional-scale models.

Moreover, the use of LiDAR as a method for the computation of riparian shading is still in its infancy and has never been used to compute the impact of riparian vegetation in a large-scale stream temperature model, during a whole annual cycle.

The goal of this paper is therefore to test the influence of shadow and sky view factor computed from LiDAR data on the simulation of maximum daily water temperature (T_{max}) with the T-NET model, a dynamic physically based model for simulating stream temperature at the regional scale using the equilibrium temperature concept. We compute SF and VF based on a LiDAR-derived raster and incorporate these data into the radiative balance of a T-NET model of the Loir River (France) (see Beaufort et al., 2016). We then compare the T_{max} simulated with LiDAR data to two other methods used in the T-NET model for computing riparian shading at the regional scales. Model validation is achieved using data from 4 temperature monitoring stations that are spread over the Loir River.

2. Methods

2.1. Principles of T-NET model

T-NET is a 1D physically-based model designed to compute water temperature along the longitudinal dimension of a hydrographic network (a GIS polyline). Reaches of this network are limited by two confluences, or by a source and a confluence (for first order reaches). T-NET was designed and applied at the regional scale (110 000 km²) by Beaufort et al. (2016). T-NET runs at an hourly time step and is based on the equilibrium temperature concept, which is defined as the water temperature at which the net rate of heat exchange at the interface of a water body is null (Bustillo et al., 2014). The model considers six fluxes [$W \cdot m^{-2}$]: net solar radiation, atmospheric longwave radiation, longwave radiation emitted from the water surface, evaporative heat flux, convective heat flux, and groundwater heat inflow. To compute these terms, the model uses the following parameters as gridded input data: air temperature [°C], specific humidity [$kg \cdot kg^{-1}$], wind velocity [$m \cdot s^{-1}$], atmospheric longwave radiation [$W \cdot m^{-2}$] and direct and diffuse solar radiation [$W \cdot m^{-2}$]. Parameters are allocated to each river reach as a function of the ratio between the length of the reach within a grid cell and the total reach length. All meteorological parameters except solar radiation are derived from the SAFRAN atmospheric reanalysis dataset (Vidal et al., 2010). These data are produced by Météo-France from both observations and modelling at an hourly time step and a spatial resolution of 8 km. Direct and diffuse solar radiation are derived from the Helioclim3-v5 dataset (Marchand et al., 2017), generated with the help of Meteosat satellite imagery at an hourly time step and a resolution of ~3×5 km. Inputs pertaining to river discharge and groundwater contributions to river flow are also required by the model. These are computed at a daily time step with the semi-distributed hydrological model EROS (Thiéry and Moutzopoulos, 1992). Both parameters are modelled at the outlets of sub-basins for which river discharge observations are available for calibration. They are then scaled to the reaches inside each sub-basin using the partial area concept. T-NET simulates longitudinal variability in water temperature between the upstream and downstream nodes of each reach, with a spatial resolution depending on the travel time (Figure 1). Water velocity is given by the ratio between discharge and channel cross-section, which is computed using the ESTIMKART empirical model developed by Lamouroux et al. (2010). At the confluence of two reaches, the output temperature is defined as the sum of the product of the

two confluences' temperature and discharge divided by the sum of the discharge of the two confluences. T-NET was thus designed to be applied on well mixed streams and not on standing waters or large estuaries, where 2D (Cole and Wells, 2006; Becker et al., 2010; Ouellet et al., 2014) or 3D models (Maderich et al., 2008) are more suitable.

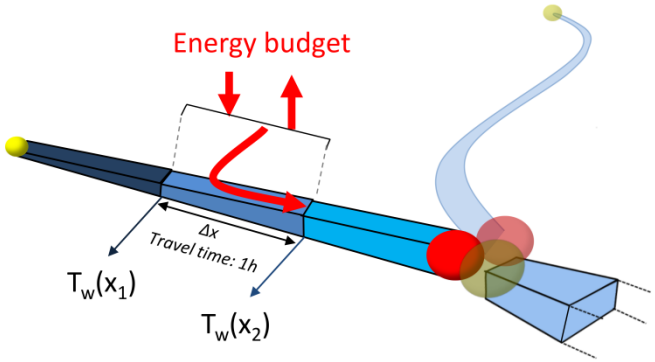

Figure 1: Principles of T-NET model

2.2. Net solar radiation calculation

In order to improve T-NET's ability to model the impact of riparian vegetation on solar radiation, modifications were made to the original model detailed by Beaufort et al. (2016). Similar to the approach of LeBlanc et al. (1997), net solar radiation (H_{ns}) is now computed as:

$$H_{ns} = R_{dir}\left(1-\alpha_{dir}\right)\left(\left(1-SF\right)+SF\,\tau\right)+R_{diff}\left(1-\alpha_{diff}\right)\left(\left(1-TVF\right)+TVF\,\tau\right) \quad \text{(Eq. 1)}$$

Where R_{dir} and R_{diff} are the direct and diffuse solar radiation [W·m^{-2}] derived from the Helioclim3-v5 product, α_{dir} and α_{diff} are the water surface albedo associated with direct and diffuse radiation respectively, τ is the transmissivity of riparian vegetation (i.e. the fraction of solar radiation that passes through the canopy), *SF* is the shadow factor and *TVF* is the tree view factor. α_{diff} was held at a constant of 0.09, following the recommendation of Sellers (1965) and α_{dir} was computed using the formulation of Anderson (1954):

$$\begin{aligned} \alpha_{dir} &= 1 && if\ \Psi < 1.24° \\ \alpha_{dir} &= 1.18 * \Psi^{-0.77} && otherwise \end{aligned} \quad \text{(Eq. 2)}$$

Where Ψ is the angle between the horizon and the sun in degrees.

τ was fixed at 50% in winter and 15% in summer. These values are the averages of global solar radiation transmissivities given by Cantón et al. (1994), Sattin et al. (1997) and Konarska et al. (2014) for deciduous tree species. Transitions between winter and summer values are described with an ascending and descending logistic regression whose equation is:

$$\tau = \frac{\kappa}{1+\exp(\pm\gamma.DoY-\beta)}+\mu \quad \text{(Eq. 3)}$$

Where *DoY* is the day of year and κ, β, γ and μ are the parameters fitted by least squares adjustment to an averaged annual cycle of ground-based NDVI measured from oak trees during 2008-2012 (Soudani et al., 2012). These trees are located in the forest of Fontainebleau (60 km to the south of Paris and ~150 km away from the centre of the Loir catchment). Data from Lebourgeois et al. (2008) indicate that, for oak trees, there is little phenologic difference between Fontainebleau and the Loir catchment. However, remote sensing observations

from Muller (1995) show that, in 1987 and in the region of Toulouse (South of France), leaf emergence of riparian trees occurs about 15 days earlier than for oaks. In order to take into account this difference between oak and riparian species, we hence considered an enlarged growing season compared to oak's phenology (β-15 days in spring, β+15 days in autumn). After fitting the four parameters on NDVI values, κ and μ, representing the upper and lower values, are adjusted to fit the winter and summer values of transmissivity (50 and 15%, respectively).

2.3.Shadow factor and view factor calculations

In order to test the influence of different riparian shading algorithms on water temperatures simulated with T-NET, we used three approaches to compute both the shadow factor (SF) and the tree view factor (TVF).

In the first approach (hereafter referred to as the *constant* method), SF and TVF are held as coefficients that are constant in time but vary as a function of Strahler order based on the equation:

$$SF = TVF = vc \times k \quad \text{(Eq. 4)}$$

where *vc* is vegetation cover (%) computed at the reach scale in a buffer of 10 m around the river, and *k* is a coefficient aiming to account for the influence of the reach width on shadow (where 1 (maximum impact) denotes a Strahler order of 1 and 0 (no impact) is associated with a Strahler order of 8). This approach is used in Beaufort et al. (2015, 2016).

In the second approach (hereafter referred to as the *variable* method), SF and TVF are derived from geometric calculations made at the reach scale, taking into account river width, tree height, vegetation cover, and position of the sun (for the shadow factor).

To compute SF at an hourly time step, the model of Li et al. (2012) was implemented in its simplest version, i.e. considering rectangular trees, located at the edge of the bank, without overhang:

$$SF = \frac{H \times \cot \Psi \times \sin \delta}{W} \times vc \quad \text{(Eq. 5)}$$

where *H* is tree height, *W* is river width, Ψ is the solar elevation angle, δ is the angle between solar azimuth and the mean azimuth [0° - 180°] of each T-NET reach (computed by considering the first and last vertices of each reach).

To compute VF, we used the second model described in Moore et al. (2014). It provides SVF for channels of infinite length, without taking into account overhanging trees. For a channel with vertical banks and fixed tree height, the width- and reach-averaged tree view factor is computed as:

$$TVF = \left[1 - \frac{0.5}{W}\left(\sqrt{H^2 + W^2} + \sqrt{H^2 + W^2} - 2H\right)\right] \times vc \quad \text{(Eq. 6)}$$

The third approach (subsequently referred to as the *lidar* method) is a spatially-explicit method that computes SF and TVF from a LiDAR-derived digital surface model (DSM). It requires a) a high-resolution digital surface model (~1 m) describing the elevation of riparian vegetation , b) information about the exact location of the river in order to define water and non-water pixels and c) polygons of river area, allowing the DSM pixels to be linked to a given T-NET reach.

To compute SF, we modified the r.sun module (Hofierka and Suri, 2002) of GRASS GIS (GRASS Development Team, 2015) to map per-pixel shade cast by the DSM. Using this algorithm, a water pixel is defined as being in shade if the elevation of the highest DSM pixel located along a 50 m track in the direction of the sun is greater than the solar elevation. Dividing the number of shaded pixels by the number of water pixels belonging to each river polygon thus provides a shadow factor for each T-NET reach. Because shading at a given hour vary slowly throughout the year, the computation was done every hour when the sun is above the horizon, every 15 days of a standard non-leap year, for every water pixel. A piecewise cubic interpolation is then applied to the SF of each hour separately in order to get a value for each day of the year.

To compute SVF from the DSM, we represented the sky as a hemisphere of radius R centred on a water pixel (as in Essery et al. (2008), Johnson and Watson (1984) and Tung et al. (2006); Figure 2). We used the r.horizon module of GRASS GIS to calculate the angle θ between the horizon and the highest DSM pixel as seen from each water pixel at horizontal azimuth steps ϕ of 10°. The whole hemisphere is thus made of n=36 segments. The diffuse radiation emission is considered to be isotropic and the river surface to be horizontal. The SVF for each segment is computed from the sphere area formula:

$$\frac{R^2\int_{\theta}^{\frac{\pi}{2}}\int_{0}^{\phi}\cos\theta\sin\theta\,d\phi\,d\theta}{R^2\int_{0}^{\frac{\pi}{2}}\int_{0}^{\phi}\cos\theta\sin\theta\,d\phi\,d\theta}=\frac{1+\cos 2\theta}{2} \qquad \text{(Eq. 7)}$$

It therefore follows that the SVF for the whole hemisphere is given by:

$$SVF=\frac{1}{2}+\frac{1}{n}\sum_{i=1}^{n}\cos 2\theta_i \qquad \text{(Eq. 8)}$$

An averaged TVF value (TVF=1-SVF) is subsequently attributed to each T-NET reach as the mean TVF value for all DSM pixels located within the reach.

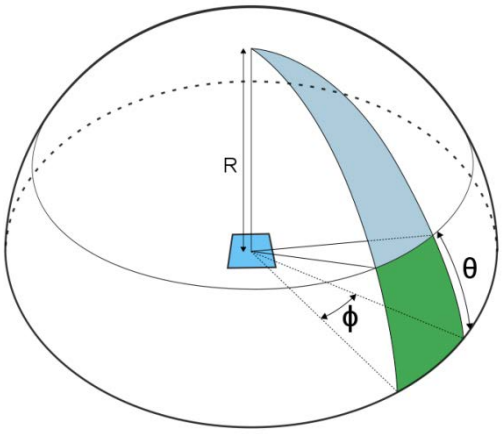

Figure 2: Calculation of a sky view factor from measures of θ, the angle between the horizon and the highest vegetation seen from a water pixel and with an angular step ϕ of 10°. R is the radius of the hemisphere

2.4.Study site and water temperature observations

The Loir River basin is an 8283 km^2 sub-catchment of the Maine River watershed located in central France (Figure 3). The river network of the Loir basin is 4420 km long, of which the Loir River itself is 316 km. The basin is generally low-lying, with altitudes ranging from 20 to 140 meters above sea level. As highlighted by the river network's variable drainage density (Figure 3), a calcareous aquifer with high permeability is present in the

north-east of the catchment. It feeds the river network with groundwater exchanges in its upstream sections (Baratelli et al., 2016). Channel slope (computed from a 25 m resolution digital terrain model of the watershed) ranges from 0.01% to 5%, with a median value of 0.5%. The main tributaries of the Loir are the Conie, the Yerre and the Aigre, with catchments areas of 530, 300 and 280 km^2 respectively. The mean discharge of the Loir at its downstream-most gauging station (1961-2015) is 31.8 $m^3 \cdot s^{-1}$ (specific discharge = 4.0 $l \cdot s^{-1} \cdot km^{-2}$). The flows of the Aigre (specific discharge = 5.4 $l \cdot s^{-1} \cdot km^{-2}$) and the Conie (specific discharge = 3.4 $l \cdot s^{-1} \cdot km^{-2}$) show little variation during the year, compared to the Loir. However, interannual fluctuations are much greater, driven by piezometric fluctuations of the Beauce aquifer.

Eighteen temperature loggers allowing for the model validation are located in the catchment. They acquired data at an hourly time step with varying periods of availability (extending from summer 2008 to summer 2014). The loggers were generally placed at a depth greater than 1 meter (according to the mean interannual water level), and steps were taken to ensure than they were installed within well-mixed sections of the channel to avoid potential stratification biases. Four of these stations are located within the main stem of the Loir (S1 to S4), where LiDAR data are available. The period of measurement is different for each station and is given in Figure 4. The annual cycle of mean daily temperature of the Loir River ranges from 2 to 24 °C at station 1 (between 08/2010 and 07/2011), while the annual amplitude of the Aigre and the Yerre are smaller because of the groundwater fluxes (5-21 °C and 4-16 °C on the same period, respectively). Temperature regime of the Conie River is strongly dependent on the groundwater level. Its variability can be similar to the Loir River (2009, 2010) or very limited (annual range of 8-14 °C in 2014).

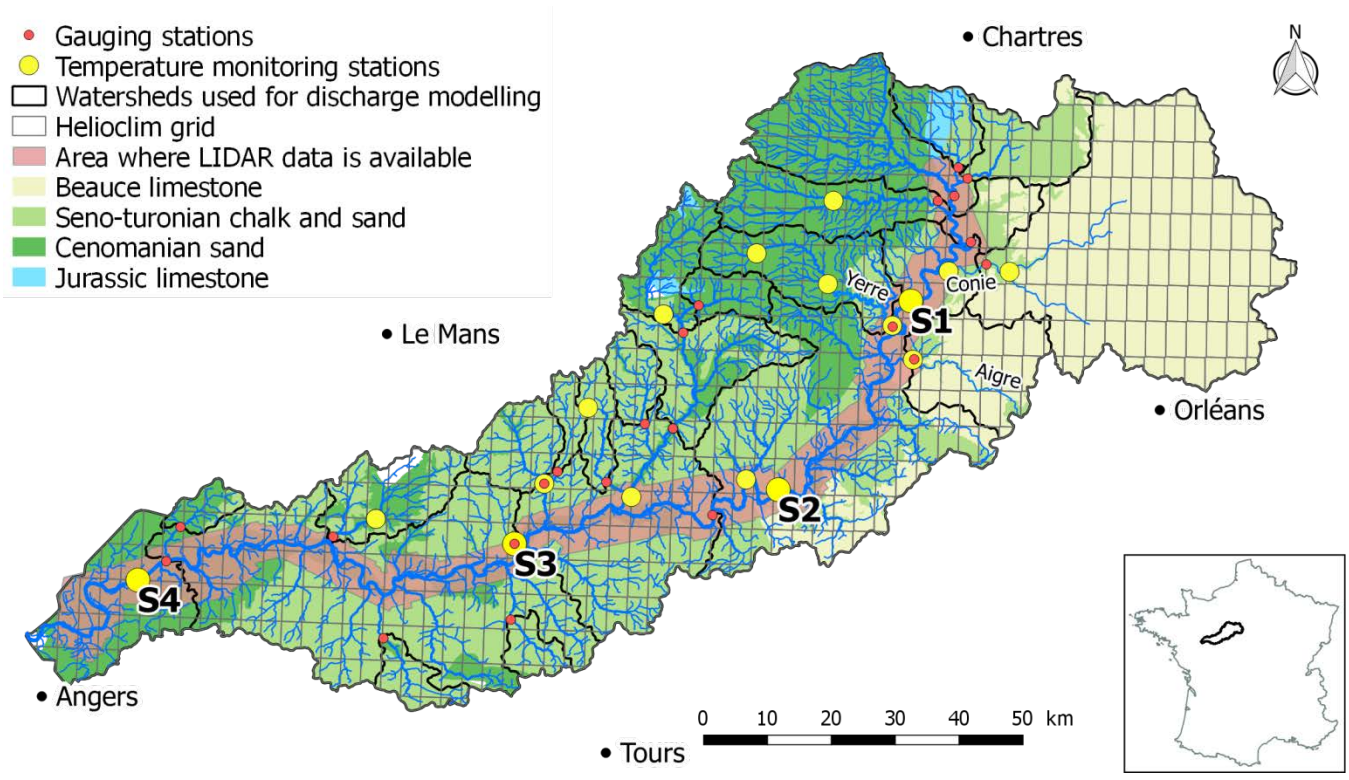

Figure 3: Map of the Loir catchment, with stream temperature monitoring stations, gauging stations, watersheds used for discharge modelling, LiDAR area, geologic formations, Helioclim grid.

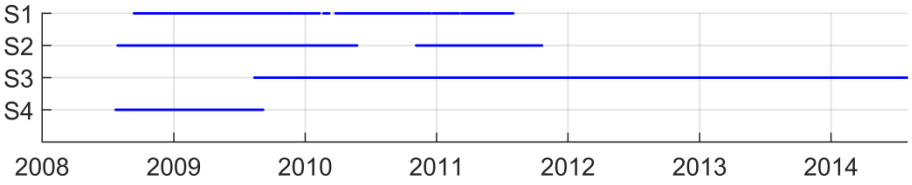

Figure 4: Period of availability of stream temperature observation at the four logger stations located on the Loir River

2.5.T-NET model implementation and criteria of model performance

The Loir River basin was implemented in the T-NET model. It consists of 2206 reaches, of which the Loir River itself is covered by 161 reaches. Simulated discharge and groundwater inputs used to drive T-NET (derived from the EROS hydrological model) were found to agree reasonably well with observed data. Nash-Sutcliffe (Nash and Sutcliffe, 1970) model efficiency coefficient (NSE) calculated against hydrometric observations ranged from 0.59 to 0.95 (1974-2012 period) for 21 of the 23 sub-basins of the Loir catchment. The remaining two sub-basins (<0.10 $m^3 \cdot s^{-1}$; located in the upper portions of the watershed) yielded negative NSE values.

In order to compare the three shading methods detailed in section 2.3, we ran the T-NET model three times on seven hydrologic years (from August 2007 to July 2014).

For the *constant* method, vegetation cover (*vc*) was derived from a dataset available at the national scale (Valette et al., 2012), which is based on river and vegetation polygons from the BD TOPO® database, provided by Institut national de l'information géographique et forestière (IGN).

For the *variable* method, *vc* was also derived from this dataset. Tree height *H* was fixed at 15m and river width *W* was estimated using the ESTIMKART empirical model (Lamouroux et al., 2010).

For the *lidar* method, the digital surface model (DSM) required for the shading computation was derived from a LiDAR survey conducted by IGN on approximately 270 km of the Loir River (85% of the total river length) on 26 May 2012. That day, average discharge was 25.5 $m^3 \cdot s^{-1}$ at the downstream-most gauging station (interannual average is 31.8 $m^3 \cdot s^{-1}$). The DSM was generated by gridding the LiDAR first returns at a resolution of 1 m^2. LiDAR accuracy was assessed as ~60 cm in the horizontal and ~20 cm in the vertical components. Because water does not reflect the LiDAR pulses, no data was available for the water pixels (unless emergent aquatic vegetation was present), and we used this property to discriminate water vs. non-water pixels inside the river polygons of the BD TOPO database. Elevations for these water pixels as well as for other sporadic data gaps were computed by attributing values from a digital elevation model (DEM) to the no data pixels. This 1-m resolution DEM, built from LiDAR final returns, provides values above water by interpolation of altitudes between the river banks. Finally, polygons from BD TOPO were also used to attribute DSM pixels to each reach of the T-NET network. Because LiDAR data were not available on the tributaries and the headwaters of the Loir, the *constant* method was applied on these reaches. With this configuration, the *lidar* method takes less than 5 hours to run on a computer with 16 CPUs and 64 Gb of RAM. Finally, in order to compare the *lidar* method with a situation without riparian vegetation, a supplementary simulation was done with SF and TVF fixed at zero everywhere.

In order to characterise differences in vegetation cover between the DSM and that derived from the BD TOPO database (Valette et al., 2012), a DEM was also used to create a raster of vegetation height by subtracting

the DEM (ground) elevations from the DSM. A vegetation cover map was then extracted from the vegetation height raster, where vegetation cover was defined as all pixels with vegetation higher than 1 m. A LiDAR-derived river width was also extracted for analysis purposes by dividing the area of water pixel inside each polygon by the length of the T-NET reaches.

Three model performance metrics were used to quantify the accuracy of the different methods regarding the maximum daily temperature. The root-mean-square error (RMSE) was used as a global performance metric:

$$RMSE = \sqrt{\frac{\sum(T_{sim} - T_{obs})^2}{N}} \quad \text{(Eq. 9)}$$

where N is the number of observations, T_{sim} is the simulated river temperature and T_{obs} is the observed river temperature. Bias (defined as the mean difference between simulated and measured temperatures) was used to quantify the mean over/underestimation of the model. Finally, the standard deviation of errors (SDE) quantifies the variability of daily biases in a given period. Because the temperature time series used for model validation were not concomitant (Figure 4), model performance was analysed using two methods. First, we compared model performance against all available validation data. This allows for comparison between the three shading methods detailed in section 2.3. Second, in order to compare spatial variability in the model's performance between the 4 temperature logger stations, we used temperature data from the period during which concurrent measures were available at all 4 stations (13th to the 31st August 2009).

3. Results

3.1. Characterisation of riparian vegetation cover

Analysis of vegetation cover extracted from the LiDAR data inside a single buffer of 10 m around the 270 km of river shows that 58% of the riparian zone is vegetated. The median vegetation height in this area is 10.0 m and the third quartile of the height (considered by Guzy et al., 2015) is 14.9 m, while the standard deviation is 6.5 m. Longitudinal profiles of vegetation cover, median and 3rd quartile of height are given in Figure 5. There is a slight but significant decreasing downstream trend for these three variables (p-value = 0.014). In comparison with the LiDAR-derived vegetation cover, vegetation cover derived from the BD TOPO database is overestimated everywhere with the exception of some small reaches (Figure 5). The median overestimation is 35% upstream of river km 160 and 22% downstream. This overestimation rises to more than 39% for 20% of the reaches.

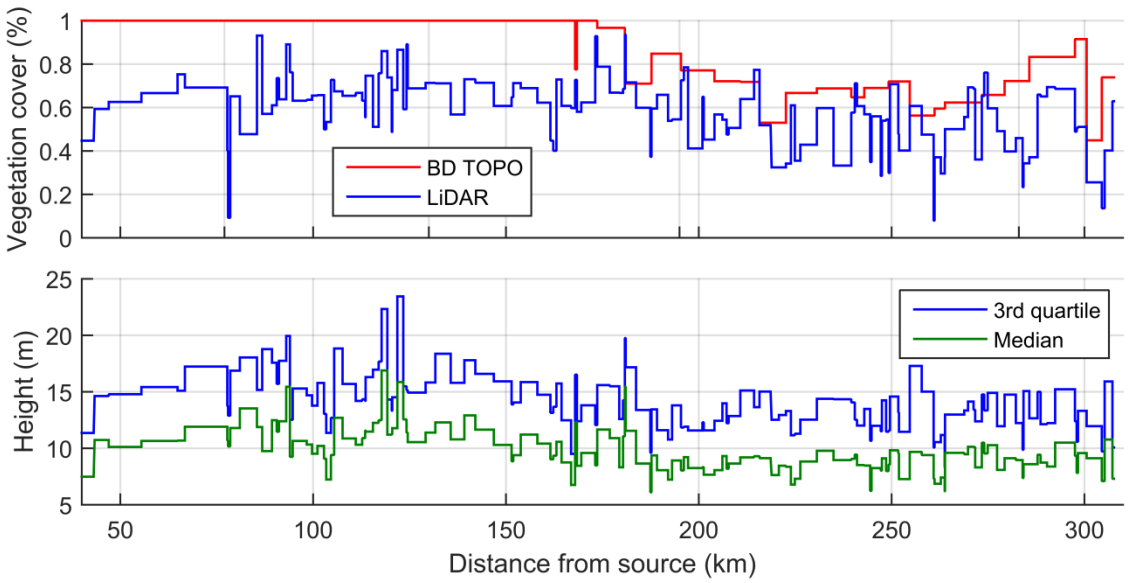

Figure 5: Characterisation of riparian vegetation for each T-NET reach (a) comparison of vegetation cover derived from the BD TOPO database (Valette et al., 2012) and LiDAR datasets (buffer of 10 m on both sides of the river polygons) (b) median and 3rd quartile vegetation heights from LiDAR data

3.2. Variation in riparian shading computed with the three methods

In the Loir catchment, direct and diffuse radiation comprise ~70% and ~30% respectively of the incoming solar radiation received at the river surface between 8 and 16h (period 2007-2014). This means that shadow factor has a greater impact on water temperature than view factor.

Figure 6 shows the longitudinal profile of SF on the Loir River for the three methods at midday on the summer solstice, when solar radiation is strongest. For the *constant* method, the reaches covered by LiDAR data have a uniform Strahler order of 5, so that the weighting coefficient *k* in this area is always equal to 0.4 (see section 2.3). The variation of SF is thus only dependent on the vegetation cover. The *variable* method varies strongly as a function of reach azimuth, even though the sun is at its highest elevation, while the *lidar* method shows smaller variations. The *lidar* method is thus less sensitive to reach azimuth, compared to the *variable* method.

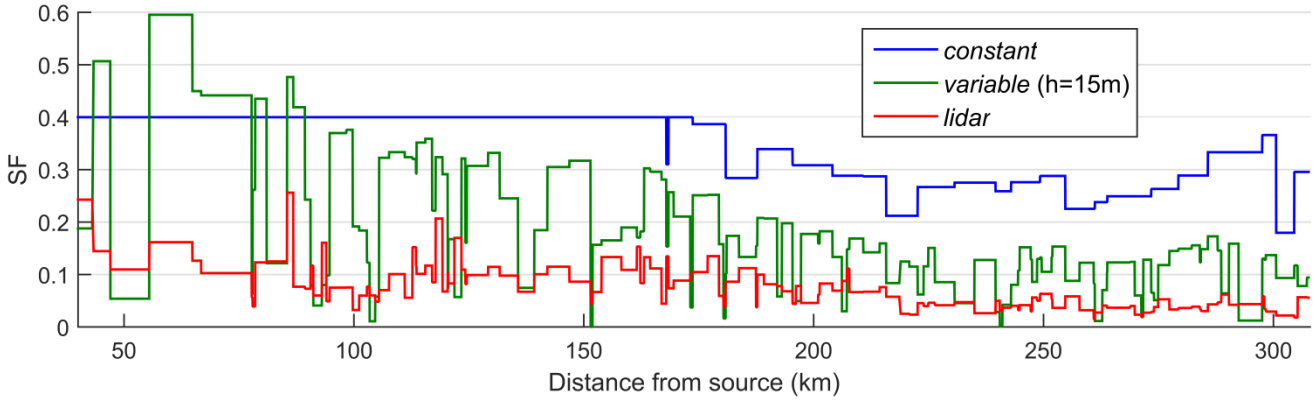

Figure 6: Longitudinal profile of shadow factor provided by the 3 methods on the Loir River at the summer solstice (21st June) at 12h UTC.

At noon, the Loir's SF computed with the *lidar* method lies between 0 and 0.3 in June (median=0.1; Figure 7a solid lines) and between 0.1 and 1 in December (median=0.5). There is thus more variability in winter than in summer, because reach azimuth has a much greater impact when the sun is low in the sky. Seasonal variability

in SF exhibits strong annual cyclicity, with SF minima centred on the summer solstice for every reach. Highest SF values are found on a reach located 85 km from the source, flowing East-West and bordered by persistent riparian forest cover (>20 m tall). Lowest SF values are found on a North-South oriented reach located 271 km from the source, explaining the weak annual cycle at noon (Figure 7a, pink solid line). Figure 7b shows the daily cycles at the summer solstice. The hour of minimum SF in a day is not always centred on noon because it depends on the reach orientation. SF obtained from the *variable* method is usually higher than that provided by the *lidar* method, except in winter and at noon for North-South oriented reaches (Figure 7a, dashed pink line). At the summer solstice, between 6 and 18h, the *variable* method yields higher SF than the *lidar* method 74% of the time, especially in the upstream parts of the watershed. Indeed, the *variable* method yields 184 occurrences of SF values equal to 1, while it only occurs 3 times with the *lidar* method.

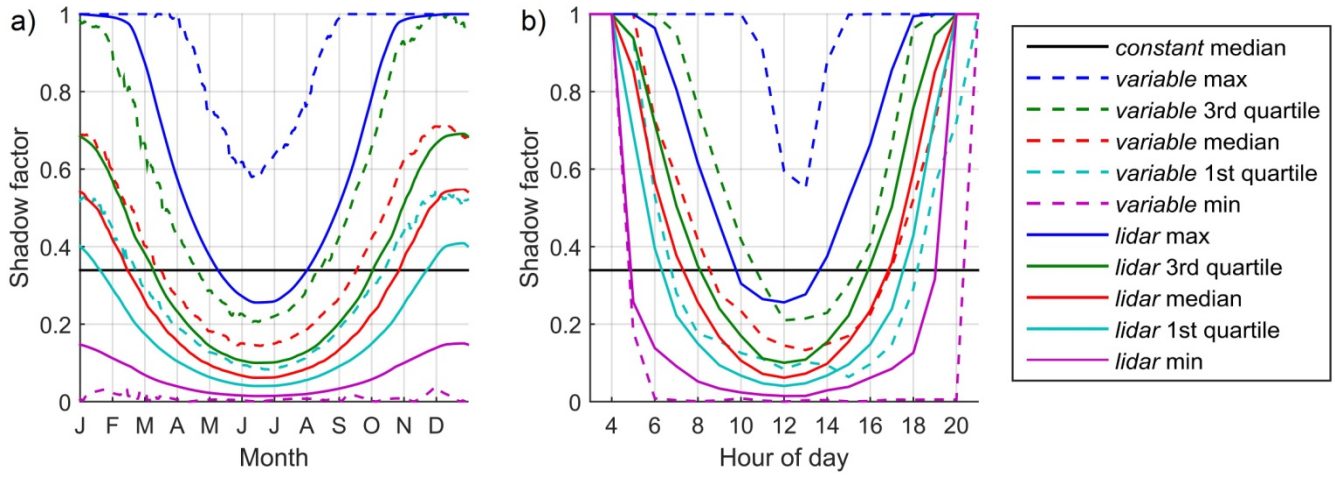

Figure 7: Percentiles of the SF distribution obtained with the three methods on the 135 T-NET reaches (a) Annual cycles at noon (b) daily cycles at the summer solstice.

Figure 8 shows the longitudinal profile of TVF for the three methods. Mean values are 0.34, 0.38 and 0.26 for the *constant*, *variable* and *lidar* methods respectively. TVF computed with the *lidar* method comprises values between 0.47 and 0.11. Like for the SF, there is a significant ($p < 0.01$) decreasing trend due to both the increasing width of the river and the decreasing vegetation cover. The *variable* method overestimates TVF, especially for the upstream portion of the river. Indeed, the inter-method variability in computed TVF values decreases as the influence of vegetation on TVF reduces with increasing river width.

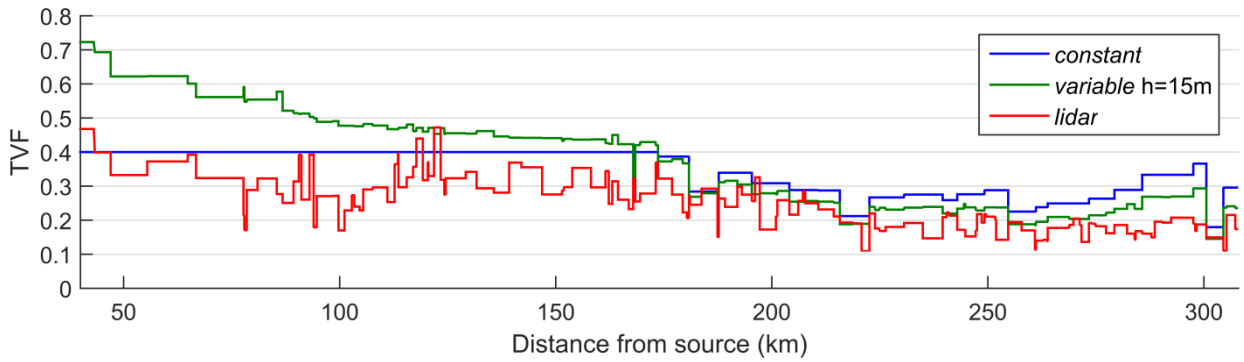

Figure 8: Longitudinal profile of tree view factor provided by the 3 methods on the Loir River. Values from the *variable* method are averaged on 08/2007-07/2014

3.3.Impact of riparian shading method on annual and seasonal river temperature simulations

366 Results of this paper focus on the 4 temperature monitoring stations located on the Loir River, where LiDAR
367 data are available. For the 14 other temperature monitoring stations located on the tributaries, the constant
368 method provides a median annual RMSE on mean daily temperature at 1.69 °C (min=1.35 °C, max=2.89 °C).
369 Seasonality in the accuracy is observed since median bias on mean daily temperature is -0.4 °C when computed
370 for the full year but rises to 0.2 °C in summer. 67% of daily biases are comprised between ±2 °C.

371 Biases, SDE and RMSE averaged on the four stations are shown in Table 1 for the April-September and the
372 October-March periods. In the April-September period, the *lidar* method improves the mean bias by 0.62 °C in
373 comparison with the *constant* method. The mean RMSE is improved by 0.22 °C although the mean SDE is
374 increased by 0.10 °C. The three metrics show that the *constant* method provides better results than the *variable*
375 method. During the October-March period, biases of the 3 methods are closer to zero. All criteria of the
376 *constant* and the *lidar* methods are very similar because solar radiation is lower and vegetation transmissivity is
377 high. However, the *variable* method is consistently colder than the other methods by ~0.3 °C.

378
379 **Table 1: Model performance criteria for maximum daily temperature, averaged for the 4 stations located on the Loir River from April to September and from October to March (°C)**

	April to September			October to March		
	Bias	SDE	RMSE	Bias	SDE	RMSE
Constant method	-1.44	1.61	2.17	-0.31	2.04	2.07
Variable method (h=15m)	-1.86	1.65	2.55	-0.60	2.09	2.18
Lidar method	-0.82	1.75	1.95	-0.33	2.05	2.08

380

381 Figure 9 shows the monthly biases (T_{sim}-T_{obs}) of maximum daily temperature (T_{max}) computed on available
382 measured data (see Figure 4). At the four stations, the *lidar* method provides improved biases in comparison to
383 both the *variable* and the *constant* method from April to September. Compared to the *variable* method, the
384 maximum improvement occurs during the spring and autumn months (2 °C at S1; 1.5 °C at S2; 0.5 °C at S3; 0.7
385 °C at S4). Despite this improvement, the *lidar* method still underestimates river temperature by more than 1 °C
386 during at least 2 months in summer at S1, S2 and S4. The *constant* method provides a consistently colder T_{max}
387 than the *variable* (and *lidar*) methods at stations 3 and 4 from May to August, presumably because this method
388 does not model the seasonal cycle of increasing and decreasing shadow length.

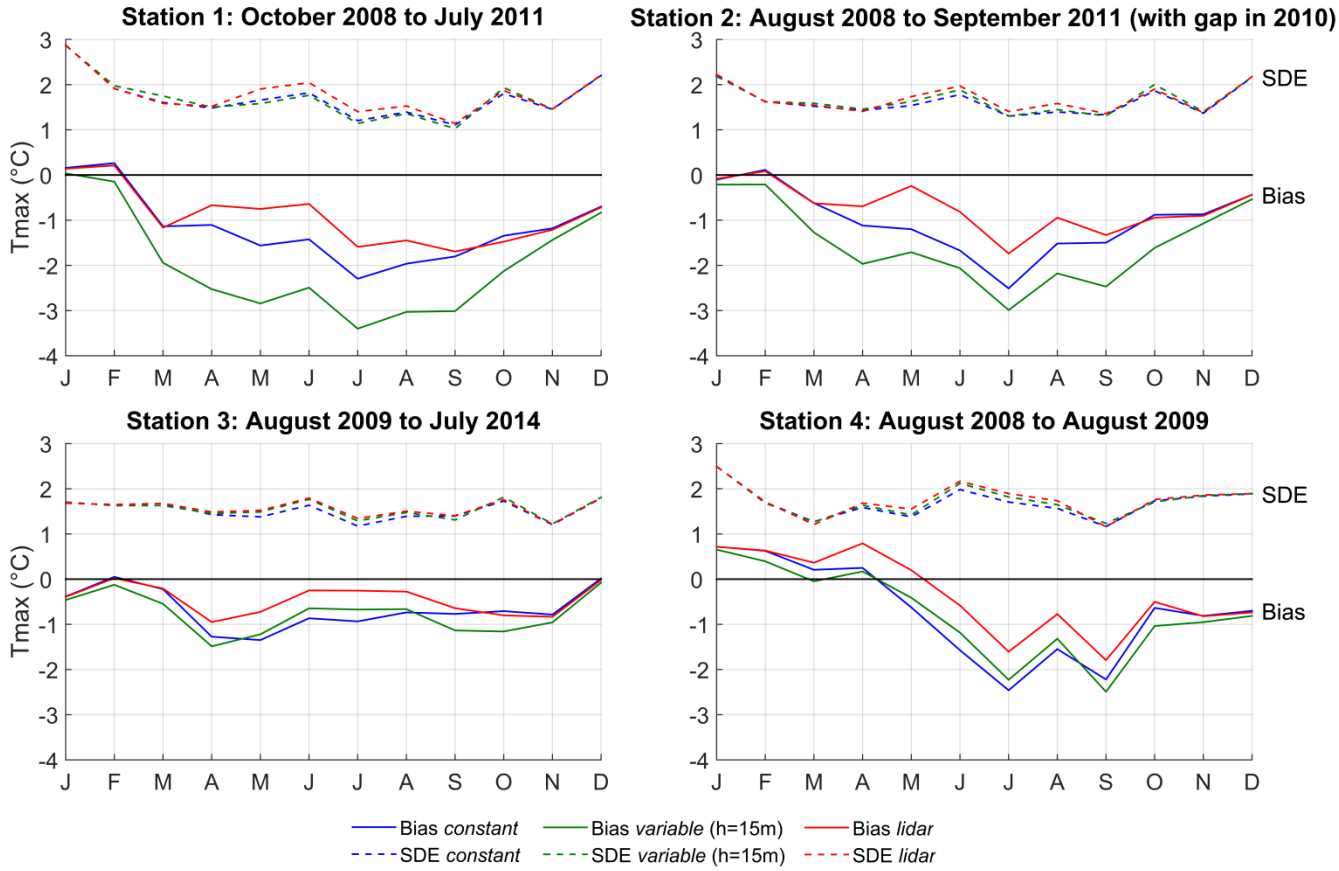

Figure 9: Monthly biases (T_{sim}-T_{obs}) and standard deviation of errors of maximum daily temperature provided by the 3 methods at the 4 stations (averaged annual cycles computed on available observed data)

Averaged annual cycles of SDE show little difference between methods and always stay above 1 °C (Figure 9). That means that simulated T_{max} is substantially more variable than observed data, whatever the method used.

3.4. Impact of riparian shading method on summer maximum daily temperature long profile

We analysed longitudinal profiles in summer by considering average maximum temperature between the 13th and the 31st August 2009. During this period, discharges were low (<7 $m^3 \cdot s^{-1}$ at the downstream-most gauging station) and the averaged maximum daily air temperature in the catchment was relatively high (25.9 °C). The longitudinal profiles (Figure 10) exhibit discontinuities in the thermal signal that are driven by cool water inflows from the Conie and Aigre rivers, which drain the Beauce aquifer (Baratelli et al., 2016). Before entering the LiDAR-covered area (shown with a dashed vertical line), the *variable* method is colder than the *constant* method by more than 2.5 °C. This difference decreases slowly in a streamwise direction until it reverses and the *variable* method becomes warmer than the *constant*. Indeed, the three methods provide a persistent warming trend as a function of distance from source, but this trend is higher for the *variable* method (1.87 °C/100 km compared to 1.23 °C/100 km and 1.25 °C/100 km for the *constant* and *lidar* methods respectively). This difference in longitudinal trend persists across all summers in the 2007-2014 simulation period. On average between the 13th and 31st August 2009, the *lidar* methods provide warmer T_{max} than the two other methods all along the Loir, with biases close to zero at stations 3 and 4. However, T_{max} is still underestimated by 1.6 and 1.3 °C at stations 1 and 2. RMSE values are 1.99, 2.08, 1.43 and 1.79 °C on S1 to S4 respectively. Figure 10 also shows the simulation considering the absence of riparian vegetation. The difference between this output and the *lidar* method

reaches up to 3.0 °C just upstream of the Conie confluence, where sensitivity analysis shows that the *lidar* method simulation is no longer under the influence of the constant method applied upstream of the LiDAR area. This difference reaches a minimal value of 1.3 °C at the downstream-most point.

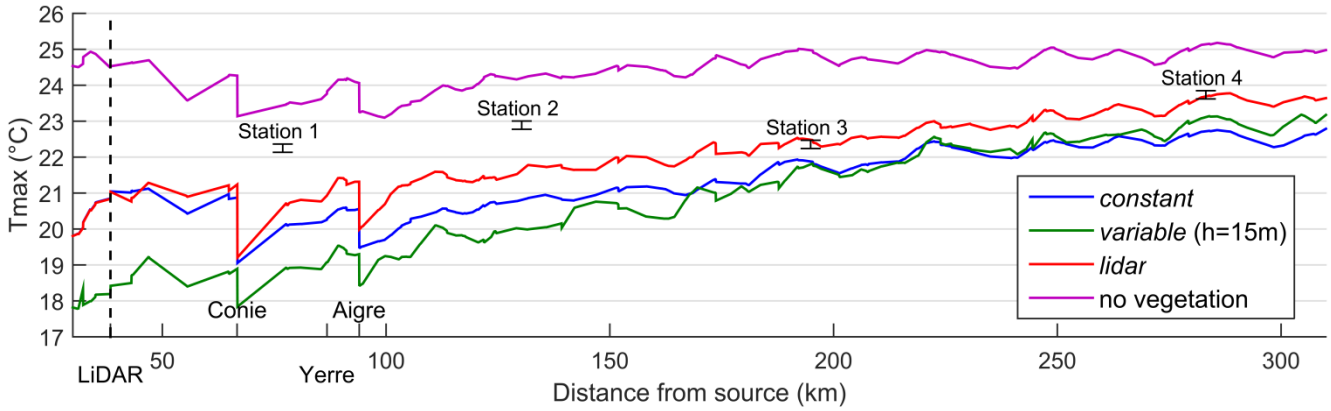

Figure 10: Longitudinal profile of maximum daily temperature (averaged between the 13 and the 31 August 2009) provided by the 3 methods and by a vegetation-free simulation. The vertical dashed line depicts the start of LiDAR cover. Conie, Yerre and Aigre are the main tributaries.

4. Discussion

4.1. Discrepancies in computed SF and TVF

The global overestimation of SF and TVF provided by the *variable* method compared to the *lidar* method can be explained by four key factors. First, the BD TOPO database that weights the results of the *variable* method clearly overestimates vegetation cover in relation to the LiDAR-derived values (discussed in section 3.1). Second, comparison of the wetted widths used in the *variable* method with LiDAR-derived river widths shows that the former are underestimated, especially upstream of ~150 km and downstream of ~250 km from the source. These width uncertainties drive an increase in SF (TVF) of 6% (4%) when averaged over the entire modelling period and 14% (9%) between 13th and 31st August 2009. Third, discrepancies may also arise from the fact that the *variable* method uses averaged stream azimuths while the *lidar* method intrinsically considers the position of vegetation in regard to the water surface. Indeed, reach azimuth impacts the timing of minimum SF (Li et al. 2012), the hourly amount of direct solar radiation and hence the maximum daily temperature (Garner et al., 2017). In order to quantify these discrepancies, we cut the Loir river GIS line in 50 m parts and compared azimuths of these small reaches with the original T-NET reaches azimuths. The mean absolute difference is 26° and R^2 is 0.66. Finally, the characterisation of vegetation cover and height at high resolution with the LiDAR data may not be reproducible in the *variable* method by taking an average of these data at the reach scale. Indeed, Greenberg et al. (2012) report that 28% of the change in insolation caused by removal of riparian vegetation characterised with LiDAR data could not be explained by considering averages at the reach scale. In our case, a multiple linear regression between LiDAR-derived TVF and LiDAR-derived tree height, vegetation cover and river width averaged at the reach scale provides R^2=0.83. Hence, 17% of the TVF variance cannot be explained by these three variables when averaged at the reach scale.

4.2. Influence of shading routine on simulated river temperatures

In order to separate the influence of the *variable* method itself from the influence of the vegetation cover data used to drive it, we injected the vegetation cover computed from the LiDAR data (10 m buffers on each river bank for each reach) into the *variable* method. As a first step, tree height was kept at 15 m. The resulting longitudinal profile (13 to 31 August 2009 average) shows that, in this configuration, the *variable* method closely approximates the *lidar* method (Figure 11). The mean bias (computed against observed temperatures) between April and September is -1.19 °C, compared to -0.94 °C for the *lidar* method and to -1.86 °C for the *variable* method with the original vegetation cover. The median vegetation height computed from the LiDAR dataset was subsequently also injected into the *variable* method. In this case, mean bias is further reduced to -0.78 °C. Using the same approach with the *constant* method provides a profile that is warmer than the *lidar* method profile prior to river km 100 and colder after river km 200. Hence, a coefficient k=0.4 seems to be appropriate for a river width of 25-30 m, during the month of August.

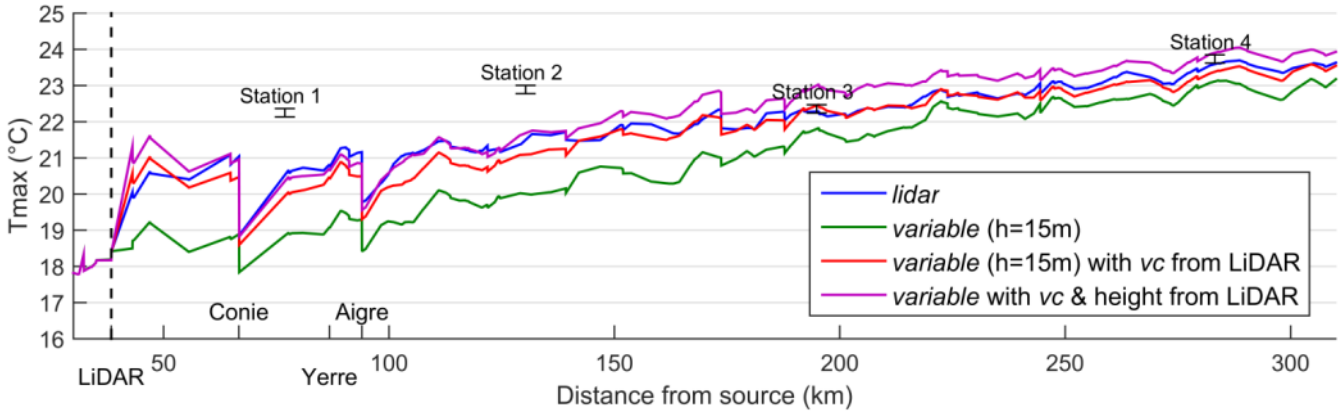

Figure 11: Longitudinal profile of maximum daily temperature (averaged between the 13 and the 31 August 2009) provided by injecting the *variable* method with vegetation cover (*vc*) and median height from LiDAR data. The vertical dashed line depicts the start of LiDAR cover. Conie, Yerre and Aigre are the main tributaries.

4.3. Performance of T-NET model on the Loir River

Although the T-NET model of the Loir River (driven with the *lidar* method) provides relatively unbiased temperature at station 3, it still underestimates temperature at stations 1 and 2 and to a lesser extent at station 4 (Figure 9). Sensitivity analyses show that uncertainty about the impact of vegetation on tributaries (because of the application of the *constant* method in areas where LiDAR data do not exist) cannot fully explain the underestimation of modelled temperatures on the Loir. Underestimation at station 1 is partly due to the underestimation of the Conie tributary. An impoundment located at the source of the river likely explains why the Conie is warmer than expected (Pedersen and Sand-Jensen, 2007; Dripps and Granger, 2013). Impoundments on several other tributaries may have the same effect and contribute to warming the Loir River and hence explain the negative biases at station 2. Station 4 is located just upstream of a small weir. There are more than 120 small weirs (height <3m) on the Loir River that may partially explain the temperature underestimation. Indeed, by increasing water depth, they increase travel time and thus sensitivity to air temperature. By decreasing water velocity, they can favour thermal stratification in summer (Torgersen et al., 2001) and since water is usually released by weir-overflow, warmer water may be selectively released. This process is not taken into account in T-NET because it only considers the longitudinal dimension. Other more complex hydrodynamic models (eg. Becker et al., 2010; Cole and Wells, 2006; Maderich et al., 2008; Deltares,

2014) would therefore be required to incorporate this process. The high temporal variability in modelled temperatures (compared to observed data) is likely due to modelled flow velocities that exceed real values. Unfortunately however, we have no observed values of travel time to compare with. Finally, it must be kept in mind that 1) computed model performances are dependent on the number of validation stations, which is limited to 4 in the current study and 2) that the T-NET model is driven with re-analysis data which are themselves subject to errors. In particular, the number of meteorological stations providing air temperature as input of the SAFRAN reanalysis in the Loir catchment is limited: approximately 10 stations are located upstream of S1 but only 2 stations located close to each other cover the rest of the basin (Quintana-Seguí et al., 2008). The density of stations is still lower for wind velocity and relative humidity but is higher for precipitations.

4.4. Implications, shading methods limitations and perspectives

Our results show that the *lidar* method has good potential for computation of SF and SVF at hourly timesteps on medium to large rivers and at large temporal and spatial scales. For small rivers (width < 10 m), whose precise location can be hard to determine using remote sensing due to obscuration by the tree canopy, the *variable* method may be more suitable, as long as it is fed with accurate vegetation cover data. Indeed, our results show that differences of modelled T_{max} can be large if the methods are used with inaccurate vegetation cover data. The quality of these input data is therefore highly important for improving stream temperature modelling. LiDAR covers of riparian zones are increasingly available, in particular because of their use for flood risk assessments. Furthermore, vegetation heights can also be obtained at the catchment scale by photogrammetric techniques (eg. Michez et al., 2017), while satellite and airborne high resolution imagery can provide accurate location of riparian vegetation (Tormos et al., 2014). These new techniques could potentially be valuable for improving future river temperature modelling efforts.

Our results show that in late August 2009, the Loir's vegetation decreases T_{max} up to 3 °C in the upstream part of the river and by 1.3 °C at the downstream-most reaches. This difference is caused by the increasing wetted width (from ~25 to ~50 m) but also by decreasing vegetation cover in the streamwise direction. These quantifications of the thermal impact of riparian vegetation are likely minimum values for two reasons. First, the impact of overhanging trees was neglected (as in all methods used in this paper) (Li et al., 2012; DeWalle, 2008). Secondly, the summer transmissivity value comes from publications studying single trees' transmissivity. However, because riparian buffers are often composed of several rows of trees, real world transmissivity values are likely to be lower, resulting in slightly cooler water temperatures (Duursma and Mäkelä, 2007; Dugdale et al., 2018). Beside this, further research is needed to validate the accuracy of shadows obtained with the *lidar* method against aerial imagery. As an example, Greenberg et al. (2012) reported an overall accuracy of 92%. Since their LiDAR data and ours were both acquired when trees were in leaf, a similar accuracy may be expected.

A wide range of values is reported in the literature regarding the cooling effect of vegetation (Moore et al., 2005), mainly for streams narrower than 10 m, for which the response of T_{max} to clear-cutting can range from 2 to 8°C (Gomi et al., 2006). For streams wider than 10 m, a modelling approach is usually used to quantify the

impacts of vegetation on stream temperature. Our results are in agreement with Woltemade and Hawkins (2016), who modelled a cooling effect of vegetation of approximately 2 °C for a 14 m wide North-West/South-East oriented stream flowing in a mountainous catchment of California (low-flow conditions). A topographic shade of 17% was considered in the deforested scenario; their result would thus be higher in an environment without mountains, like the Loir catchment. Using LiDAR data, Wawrzyniak et al. (2017) modelled a cooling impact of 0.4 °C on T_{max} on a 22 km-long groundwater-fed river reach with a wetted width ranging from 50 to 120 m. The overall NNE-SSW orientation of this river is likely to decrease the impact of riparian vegetation, in comparison with the Loir, which is globally east-west orientated. Other studies show that the impact of vegetation decreases steadily as wetted width increases to about 30 m (Teti, 2006), 10 m (Davies-Colley and Quinn, 1998) and 17 to 43 m for East-West to North-South oriented streams (DeWalle, 2008). Our results suggest that the cooling effect can remain above 1 °C even for widths larger than 40 m.

Potential improvements to our *lidar* method include the incorporation of wetted widths related to the discharge. Although this is possible at small spatial and temporal scales by using a hydraulic model (Wawrzyniak et al., 2017), modelling wetted widths at regional scales can be very complex, especially without field measures of hydraulic geometry. Channel morphology from bathymetric LiDAR data may be one potential solution to this issue (eg. Hilldale and Raff, 2008; Bailly et al., 2010). Another potential improvement to our methodology relates to the use of Beer's law to model the extinction of solar rays through the tree canopy, as demonstrated by several investigations using coarse vegetation data (Sun et al., 2015; Tung et al., 2007; Sridhar et al., 2004; Lee et al., 2012). Transmission of light beneath the canopy of overhanging trees could also be modelled, but requires information or hypotheses regarding the shape of trees. When aerial imagery is available, more complex methods considering position of individual trees may be used in order to model the transmission of light beneath the canopy (Essery et al., 2008).

Finally, this paper focuses on the impact of vegetation on solar radiation and hence on maximum daily temperature (Johnson, 2004; Garner et al., 2017). Although the impact of vegetation on longwave radiation is limited on sunny days (Leach and Moore, 2010; DeWalle, 2008), view factors computed in this paper could be used to quantify the impact of vegetation on longwave fluxes at both regional scales and during a complete annual cycle. LiDAR data could also be used to model the impact of vegetation on water temperature resulting from decreased air temperature and wind velocity engendered by the riparian canopy. Indeed, forest canopies can reduce daytime air temperature by 3 °C to more than 6 °C and wind velocity by 10-20 % in comparison with open areas (Moore et al., 2005).

5. Conclusion

The main goal of this study was to understand the influence of using a LiDAR-derived digital surface model to quantify the impact of riparian vegetation on 270 km of the Loir River. We demonstrated that the use of LiDAR data improves the mean biases of simulated maximum daily temperatures (T_{max}) in summer, compared to two other simpler methods for computing the effects of riparian shading at large scales. However, it did not improve

548 the standard deviation of errors on T_{max}, which is likely more influenced by the presence of weirs and
549 impoundments.
550 The monthly-averaged difference in T_{max} computed by the various shading methods can reach up to 2 °C at the
551 upstream-most station and 1 °C at the downstream-most station. However, this difference is mainly due to the
552 overestimation of vegetation cover in the dataset used to compute shadow and view factors in the non-*lidar*
553 methods. Indeed, injection of vegetation cover extracted from the LiDAR data into the shading method of
554 medium complexity (*variable method*) decreased the largest difference at the upstream-most station to 0.8 °C,
555 suggesting that this method is sufficient for the computation of SF and VF provided that it is supplied with
556 accurate (high-resolution) data pertaining to vegetation cover. Improving the quality of riparian vegetation data
557 should therefore be a priority for improving stream temperature modelling at the regional scale. The simplest
558 method (*constant* method) may be appropriate to model mean daily temperature for a given period of the year,
559 as long as vegetation cover is weighted with a coefficient depending on the river width.
560 We hope that the application and comparison of methods demonstrated in this paper will improve
561 understanding of the strengths and limitations of other existing stream temperature models. Enhancing the
562 ability of models to simulate the impact of riparian vegetation is of key importance for the development of
563 climate change adaptation measures and understanding the fundamental processes responsible for spatio-
564 temporal variability of river temperature.
565

566 ## Acknowledgements

567 This work forms part of a PhD thesis project supported by Agence française pour la biodiversité. Thanks are due
568 to Météo-France for the SAFRAN database, to Transvalor for the Helioclim data, to D. Thiéry for the hydrological
569 modelling, to A. Chandesris for the vegetation database, to K. Soudani for the NDVI data, to Direction régionale
570 de l'environnement, de l'aménagement et du logement Pays de la Loire and to Fédération Départementale de
571 Pêche d'Eure et Loir for the temperature data. This paper was improved thanks to the comments of two
572 anonymous reviewers. We also thank the CaSciModOT federation (Calcul Scientifique et Modélisation Orléans
573 Tours) as well as Yves Lansac and Enrick Olive (GREMAN UMR 7347) for providing the computing resources.
574

References

Anderson E. R. (1954) Energy budget studies, Part of Water Loss Investigations—Lake Hefner Studies. *US Geological Survey. Professional Paper*, 269.

Bailly J.-S., Le Coarer Y., Languille P., Stigermark C.-J., Allouis T. (2010) Geostatistical estimations of bathymetric LiDAR errors on rivers. *Earth Surface Processes and Landforms*, 35 (10), 1199–1210.

Baratelli F., Flipo N., Moatar F. (2016) Estimation of stream-aquifer exchanges at regional scale using a distributed model: Sensitivity to in-stream water level fluctuations, riverbed elevation and roughness. *Journal of Hydrology*, 542, 686–703.

Beaufort A., Curie F., Moatar F., Ducharne A., Melin E., Thiery D. (2016) T-NET, a dynamic model for simulating daily stream temperature at the regional scale based on a network topology. *Hydrological Processes*, 2196-2210.

Beaufort A., Moatar F., Curie F., Ducharne A., Bustillo V., Thiéry D. (2015) River Temperature Modelling by Strahler Order at the Regional Scale in the Loire River Basin, France. *River Research and Applications*, 597-609.

Becker A., Kirchesch V., Baumert H. Z., Fischer H., Schöl A. (2010) Modelling the effects of thermal stratification on the oxygen budget of an impounded river. *River Research and Applications*, 26 (5), 572–588.

Boisneau C., Moatar F., Bodin M., Boisneau P. (2008) Does global warming impact on migration patterns and recruitment of Allis shad (Alosa alosa L.) young of the year in the Loire River, France? *Hydrobiologia*, 602 (1), 179–186.

Bustillo V., Moatar F., Ducharne A., Thiéry D., Poirel A. (2014) A multimodel comparison for assessing water temperatures under changing climate conditions via the equilibrium temperature concept: case study of the Middle Loire River, France. *Hydrological Processes*, 28 (3), 1507–1524.

Cantón M. A., Cortegoso J. L., Rosa C. de. (1994) Solar permeability of urban trees in cities of western Argentina. *Energy and Buildings*, 20 (3), 219–230.

Chen Y. D., Carsel R. F., McCutcheon S. C., Nutter W. L. (1998) Stream Temperature Simulation of Forested Riparian Areas: I. Watershed-Scale Model Development. *Journal of Environmental Engineering*, 124 (4), 304–315.

Cheng S.-T., Wiley M. J. (2016) A Reduced Parameter Stream Temperature Model (RPSTM) for basin-wide simulations. *Environmental Modelling & Software*, 82, 295–307.

Cole T., Wells S. (2006) CE-QUAL-W2: A Two-dimensional, Laterally Averaged, Hydrodynamic and Water Quality Model, Version 3.5. *Civil and Environmental Engineering Faculty Publications and Presentations*. Retrieved from http://pdxscholar.library.pdx.edu/cengin_fac/130

Cox M. M., Bolte J. P. (2007) A spatially explicit network-based model for estimating stream temperature distribution. *Environmental Modelling & Software* Special section: Environmental Risk and Emergency Management, 22 (4), 502–514.

Davies-Colley R. J., Quinn J. M. (1998) Stream lighting in five regions of North Island, New Zealand: Control by channel size and riparian vegetation. *New Zealand Journal of Marine and Freshwater Research*, 32 (4), 591–605.

Deltares. (2014) Delft3D-FLOW: Simulation of Multidimensional Hydrodynamic Flows and Transport Phenomena, including Sediments, User Manual. *Deltares Systems, Delft, The Netherlands, 684 pp*.

DeWalle D. R. (2008) Guidelines for Riparian Vegetative Shade Restoration Based Upon a Theoretical Shaded-Stream Model. *JAWRA Journal of the American Water Resources Association*, 44 (6), 1373–1387.

Dripps W., Granger S. R. (2013) The impact of artificially impounded, residential headwater lakes on downstream water temperature. *Environmental Earth Sciences*, 68 (8), 2399–2407.

Dugdale S. J., Malcolm I. A., Kantola K., Hannah D. M. (2018) Stream temperature under contrasting riparian forest cover: Understanding thermal dynamics and heat exchange processes. *Science of The Total Environment*, 610, 1375–1389.

Duursma R. A., Mäkelä A. (2007) Summary models for light interception and light-use efficiency of non-homogeneous canopies. *Tree Physiology*, 27 (6), 859–870.

Essery R., Bunting P., Rowlands A., Rutter N., Hardy J., Melloh R., Link T., et al. (2008) Radiative Transfer Modeling of a Coniferous Canopy Characterized by Airborne Remote Sensing. *Journal of Hydrometeorology*, 9 (2), 228–241.

Fu P., Rich P. M. (1999) Design and implementation of the Solar Analyst: an ArcView extension for modeling solar radiation at landscape scales. *Proceedings of the Nineteenth Annual ESRI User Conference*, 1–31.

Garner G., Malcolm I. A., Sadler J. P., Hannah D. M. (2014) What causes cooling water temperature gradients in a forested stream reach? *Hydrology and Earth System Sciences*, 18 (12), 5361–5376.

Garner G., Malcolm I. A., Sadler J. P., Hannah D. M. (2017) The role of riparian vegetation density, channel orientation and water velocity in determining river temperature dynamics. *Journal of Hydrology*. Retrieved from http://www.sciencedirect.com/science/article/pii/S0022169417301695

Gomi T., Moore R. D., Dhakal A. S. (2006) Headwater stream temperature response to clear-cut harvesting with different riparian treatments, coastal British Columbia, Canada. *Water Resources Research*, 42 (8), W08437.

GRASS Development Team. (2015) Geographic Resources Analysis Support System (GRASS GIS) Software, Version 7.1; Open Source Geospatial Foundation. Retrieved from http://grass.osgeo.org

Greenberg J. A., Hestir E. L., Riano D., Scheer G. J., Ustin S. L. (2012) Using LiDAR Data Analysis to Estimate Changes in Insolation Under Large-Scale Riparian Deforestation. *JAWRA Journal of the American Water Resources Association*, 48 (5), 939–948.

Guzy M., Richardson K., Lambrinos J. G. (2015) A tool for assisting municipalities in developing riparian shade inventories. *Urban Forestry & Urban Greening*, 14 (2), 345–353.

Haag I., Luce A. (2008) The integrated water balance and water temperature model LARSIM-WT. *Hydrological Processes*, 22 (7), 1046–1056.

Haag I., Westrich B. (2002) Processes governing river water quality identified by principal component analysis. *Hydrological Processes*, 16 (16), 3113–3130.

Hannah D., Garner G. (2015) River water temperature in the United Kingdom: Changes over the 20th century and possible changes over the 21st century. *Progress in Physical Geography*, 39, 68-92.

Hilldale R. C., Raff D. (2008) Assessing the ability of airborne LiDAR to map river bathymetry. *Earth Surface Processes and Landforms*, 33 (5), 773–783.

Hofierka J., Suri M. (2002) The solar radiation model for Open source GIS: implementation and applications. *Proceedings of the Open source GIS-GRASS users conference*, 1–19.

Johnson G. T., Watson I. D. (1984) The Determination of View-Factors in Urban Canyons. *Journal of Climate and Applied Meteorology*, 23 (2), 329–335.

Johnson M. F., Wilby R. L. (2015) Seeing the landscape for the trees: Metrics to guide riparian shade management in river catchments. *Water Resources Research*, 51 (5), 3754–3769.

Johnson S. L. (2004) Factors influencing stream temperatures in small streams: substrate effects and a shading experiment. *Canadian Journal of Fisheries and Aquatic Sciences*, 61 (6), 913–923.

Konarska J., Lindberg F., Larsson A., Thorsson S., Holmer B. (2014) Transmissivity of solar radiation through crowns of single urban trees - application for outdoor thermal comfort modelling. *Theoretical and Applied Climatology*, 117 (3–4), 363–376.

Lalot E., Curie F., Wawrzyniak V., Schomburgk S., Piegay H., Moatar F. (2015) Quantification of the Beauce's Groundwater contribution to the Loire River discharge using satellite infrared imagery. *Hydrol. Earth Syst. Sci. Discuss.*, 12 (2), 2047–2080.

Lamouroux N., Pella H., Vanderbecq A., Sauquet E., Lejot J. (2010) Estimkart 2.0: Une plate-forme de modèles écohydrologiques pour contribuer à la gestion des cours d'eau à l'échelle des bassins français. Version provisoire. *Version provisoire. Cemagref, Agence de l'Eau Rhône-Méditerranée-Corse, Onema, Lyon (45 pp.)*.

Leach J., Moore R. (2010) Above-stream microclimate and stream surface energy exchanges in a wildfire-disturbed riparian zone. *Hydrological Processes*, 24 (17), 2369–2381.

LeBlanc R. T., Brown R. D., FitzGibbon J. E. (1997) Modeling the Effects of Land Use Change on the Water Temperature in Unregulated Urban Streams. *Journal of Environmental Management*, 49 (4), 445–469.

Lebourgeois F., Pierrat J.-C., Perez V., Piedallu C., Cecchini S., Ulrich E. (2008) Phenological timing in French temparate forests - A study on stands in the Renecofor network. Retrieved from http://hdl.handle.net/2042/19767

Lee T. Y., Huang J. C., Kao S. J., Liao L. Y., Tzeng C. S., Yang C. H., Kalita P. K., et al. (2012) Modeling the effects of riparian planting strategies on stream temperature: Increasing suitable habitat for endangered Formosan Landlocked Salmon in Shei-Pa National Park, Taiwan. *Hydrological Processes*, 26 (24), 3635–3644.

Li G., Jackson C. R., Kraseski K. A. (2012) Modeled riparian stream shading: Agreement with field measurements and sensitivity to riparian conditions. *Journal of Hydrology*, 428, 142–151.

685 Loinaz M. C., Davidsen H. K., Butts M., Bauer-Gottwein P. (2013) Integrated flow and temperature modeling at
686 the catchment scale. *Journal of Hydrology*, 495, 238–251.
687 Maderich V., Heling R., Bezhenar R., Brovchenko I., Jenner H., Koshebutskyy V., Kuschan A., et al. (2008)
688 Development and application of 3D numerical model THREETOX to the prediction of cooling water
689 transport and mixing in the inland and coastal waters. *Hydrological Processes*, 22 (7), 1000–1013.
690 Magnuson J. J., Crowder L. B., Medvick P. A. (1979) Temperature as an Ecological Resource. *American Zoologist*,
691 19 (1), 331–343.
692 Marchand M., Al-Azri N., Ombe-Ndeffotsing A., Wey E., Wald L. (2017) Evaluating meso-scale change in
693 performance of several databases of hourly surface irradiation in South-eastern Arabic Pensinsula.
694 *Advances in Science and Research*, 14, 7.
695 Michez A., Piégay H., Lejeune P., Claessens H. (2017) Multi-temporal monitoring of a regional riparian buffer
696 network (>12,000 km) with LiDAR and photogrammetric point clouds. *Journal of Environmental*
697 *Management* Piégay & Lamouroux "Enlarging spatial and temporal scales for biophysical diagnosis and
698 sustainable river management," 202 (Part 2), 424–436.
699 Moatar F., Gailhard J. (2006) Water temperature behaviour in the River Loire since 1976 and 1881. *Comptes*
700 *Rendus Geoscience*, 338 (5), 319–328.
701 Moatar F., Miquel J., Poirel A. (2001) A quality-control method for physical and chemical monitoring data.
702 Application to dissolved oxygen levels in the river Loire (France). *Journal of Hydrology*, 252 (1–4), 25–36.
703 Moore R. D., Leach J. A., Knudson J. M. (2014) Geometric calculation of view factors for stream surface radiation
704 modelling in the presence of riparian forest. *Hydrological Processes*, 28 (6), 2975–2986.
705 Moore R. D., Spittlehouse D. L., Story A. (2005) Riparian Microclimate and Stream Temperature Response to
706 Forest Harvesting: A Review. *JAWRA Journal of the American Water Resources Association*, 41 (4), 813–
707 834.
708 Muller E. (1995) Phénologie forestière révélée par l'analyse d'images thematic mapper. *Comptes rendus de*
709 *l'Académie des sciences. Série 3, Sciences de la vie*, 318 (9), 993–1003.
710 Nash J. E., Sutcliffe J. V. (1970) River flow forecasting through conceptual models part I — A discussion of
711 principles. *Journal of Hydrology*, 10 (3), 282–290.
712 Ouellet V., Secretan Y., St-Hilaire A., Morin J. (2014) Daily Averaged 2d Water Temperature Model for the St.
713 Lawrence River. *River Research and Applications*, 30 (6), 733–744.
714 Pedersen N. L., Sand-Jensen K. (2007) Temperature in lowland Danish streams: contemporary patterns,
715 empirical models and future scenarios. *Hydrological Processes*, 21 (3), 348–358.
716 Quintana-Seguí P., Le Moigne P., Durand Y., Martin E., Habets F., Baillon M., Canellas C., et al. (2008) Analysis of
717 near-surface atmospheric variables: Validation of the SAFRAN analysis over France. *Journal of applied*
718 *meteorology and climatology*, 47 (1), 92–107.
719 Sattin M., Milne R., Deans J. D., Jarvis P. G. (1997) Radiation interception measurement in poplar: sample size
720 and comparison between tube solarimeters and quantum sensors. *Agricultural and Forest Meteorology*,
721 85 (3–4), 209–216.
722 Sellers W. D. (1965) Physical climatology; University of Chicago Press.
723 Soudani K., Hmimina G., Delpierre N., Pontailler J.-Y., Aubinet M., Bonal D., Caquet B., et al. (2012) Ground-
724 based Network of NDVI measurements for tracking temporal dynamics of canopy structure and
725 vegetation phenology in different biomes. *Remote Sensing of Environment*, 123, 234–245.
726 Sridhar V., Sansone A. L., LaMarche J., Dubin T., Lettenmaier D. P. (2004) Prediction of stream temperature in
727 forested watersheds; Wiley Online Library.
728 Sun N., Yearsley J., Voisin N., Lettenmaier D. P. (2015) A spatially distributed model for the assessment of land
729 use impacts on stream temperature in small urban watersheds. *Hydrological Processes*, 29 (10), 2331–
730 2345.
731 Teti P. (2006) Stream shade as a function of channel width and riparian vegetation in the BC southern interior.
732 Streamline Watershed Manag. *Bull*, (9), 10–15.
733 Thiéry D., Moutzopoulos C. (1992) Un modele hydrologique spatialisé pour la simulation de tres grands bassins:
734 le modele EROS formé de grappes de modeles globaux élémentaires. *VIIIèmes journées hydrologiques*
735 *de l'ORSTOM: Régionalisation en hydrologie, application au développement*, 285–295; ORSTOM
736 Editions.
737 Torgersen C. E., Faux R. N., McIntosh B. A., Poage N. J., Norton D. J. (2001) Airborne thermal remote sensing for
738 water temperature assessment in rivers and streams. *Remote Sensing of Environment*, 76 (3), 386–398.
739 Tormos T., Van Looy K., Villeneuve B., Kosuth P., Souchon Y. (2014) High resolution land cover data improve
740 understanding of mechanistic linkages with stream integrity. *Freshwater Biology*, 59 (8), 1721–1734.

741 Tung C.-P., Lee T.-Y., Yang Y.-C. (2006) Modelling climate-change impacts on stream temperature of Formosan
742 landlocked salmon habitat. *Hydrological Processes*, 20 (7), 1629–1649.
743 Tung C.-P., Yang Y.-C. E., Lee T.-Y., Li M.-H. (2007) Modification of a stream temperature model with Beer's law
744 and application to GaoShan Creek in Taiwan. *Ecological Modelling*, 200 (1–2), 217–224.
745 Valette L., Piffady J., Chandesris A., Souchon Y. (2012) SYRAH-CE: description des données et modélisation du
746 risque d'altération de l'hydromorphologie des cours d'eau pour l'Etat des lieux DCE. *Rapport final, Pôle*
747 *Hydroécologie des cours d'eau Onema-Irstea Lyon, MALY-LHQ, Lyon*.
748 Vidal J.-P., Martin E., Franchistéguy L., Baillon M., Soubeyroux J.-M. (2010) A 50-year high-resolution
749 atmospheric reanalysis over France with the Safran system. *International Journal of Climatology*, 30
750 (11), 1627–1644.
751 Wawrzyniak V., Allemand P., Bailly S., Lejot J., Piégay H. (2017) Coupling LiDAR and thermal imagery to model
752 the effects of riparian vegetation shade and groundwater inputs on summer river temperature. *Science*
753 *of The Total Environment*, 592 (Supplement C), 616–626.
754 Woltemade C. J., Hawkins T. W. (2016) Stream Temperature Impacts Because of Changes in Air Temperature,
755 Land Cover and Stream Discharge: Navarro River Watershed, California, USA. *River Research and*
756 *Applications*, 32 (10), 2020–2031.
757